Bone Reports 15 (2021) 101100

Contents lists available at ScienceDirect

Bone Reports

journal homepage: www.elsevier.com/locate/bonr

Ectopic mineralisation of the mandibular symphysis in *ENT1* knockout mice: A model of dystrophic calcification

Dale E. Fournier [a,b,1], Kim L. Beaucage [c,d,1], Ryan J. Beach [d], Patti K. Kiser [e], Cheryle A. Séguin [b,d,*,2], S. Jeffrey Dixon [b,c,d,2]

[a] Health and Rehabilitation Sciences, Faculty of Health Sciences, The University of Western Ontario, London, Ontario, Canada
[b] Bone and Joint Institute, The University of Western Ontario, London, Ontario, Canada
[c] Dentistry, Schulich School of Medicine & Dentistry, The University of Western Ontario, London, Ontario, Canada
[d] Department of Physiology and Pharmacology, Schulich School of Medicine & Dentistry, The University of Western Ontario, London, Ontario, Canada
[e] Department of Pathology and Laboratory Medicine, Schulich School of Medicine & Dentistry, The University of Western Ontario, London, Ontario, Canada

ARTICLE INFO

Keywords:
Adenosine transporter
Diffuse idiopathic skeletal hyperostosis
Disease models, animal
Equilibrative nucleoside transporter 1
X-ray diffraction
X-ray microtomography

ABSTRACT

Equilibrative nucleoside transporter 1 (ENT1) transfers nucleosides, such as adenosine, across plasma membranes. We reported previously that mice lacking ENT1 (*ENT1*$^{-/-}$) exhibit progressive ectopic calcification of spinal tissues—a phenotype resembling diffuse idiopathic skeletal hyperostosis (DISH) in humans. Our objective was to investigate potential calcification of orofacial tissues in *ENT1*$^{-/-}$ mice. Heads of wild-type mice and *ENT1*$^{-/-}$ mice from 3 to 17 months were evaluated using microcomputed tomography (μCT). Some heads were decalcified and processed for histological assessment. Other heads were examined using energy dispersive X-ray spectroscopy and micro X-ray diffraction. Using μCT, *ENT1*$^{-/-}$ mice showed extensive radiopaque lesions within the mandibular symphysis, the severity of which increased with advancing age. Histologically, at 6 months these ectopic radiopacities were found to correspond to acellular, amorphous, eosinophilic material, with no evidence of inflammatory cells. Because lesions were localised to the symphysis, we identified early pathological changes at 3 months and observed that lesions initiated specifically within the fibrocartilage pad. Energy-dispersive X-ray spectroscopy of ectopic lesions revealed large amounts of calcium and phosphorous in a molar ratio of ~1.59, and X-ray diffraction profiles matched that of calcium-deficient hydroxyapatite. This is the first characterisation of ectopic calcifications within the mandibular symphysis of *ENT1*$^{-/-}$ mice, indicating a role for ENT1 and adenosine metabolism in regulating calcification of fibrocartilaginous tissues. Moreover, these murine lesions resemble areas of dystrophic calcification in the spinal tissues of humans with DISH. Importantly, ectopic calcifications develop in a reproducible temporal pattern within a well-defined anatomical region and, thus, provide a model for determining the cellular and molecular pathways underlying ectopic calcification in DISH and related disorders.

1. Introduction

In humans, there are a number of disorders that involve the ectopic deposition of mineral (Giachelli, 1999; Li et al., 2014). One such disorder is diffuse idiopathic skeletal hyperostosis (DISH), which involves mineralisation of the connective tissues of the spine (Forestier and Rotes-Querol, 1950). The prevalence of DISH is estimated to be 15 to 20% of the population over 50 years of age, based on outpatient studies (Weinfeld et al., 1997; Westerveld et al., 2008). The clinical diagnosis of DISH in humans is based on radiographic features: (i) flowing mineral along at least four consecutive motion segments; (ii) preserved intervertebral disc space in involved regions; and (iii) absence of vertebral facet or sacro-iliac erosion, sclerosis, or fusion (Resnick and Niwayama, 1976). The etiology of DISH is unknown and there are no disease-modifying treatments beyond surgical resection of the problematic mineralised tissue (Mader et al., 2013). This underscores the need to

* Corresponding author at: Department of Physiology and Pharmacology, Schulich School of Medicine & Dentistry, The University of Western Ontario, London, Ontario N6A 5C1, Canada.
E-mail address: cheryle.seguin@schulich.uwo.ca (C.A. Séguin).
[1] These authors contributed equally and are co-first authors.
[2] These authors are co-senior authors.

https://doi.org/10.1016/j.bonr.2021.101100
Received 16 January 2021; Received in revised form 7 May 2021; Accepted 15 June 2021
Available online 18 June 2021

characterise the tissue types and cellular changes associated with ectopic mineralisation. A preclinical model would be extremely useful for investigating pathogenesis and testing potential therapeutics for DISH and related disorders.

In this regard, our group has previously characterised a murine model of progressive ectopic calcification that involves spinal and sternal tissues (Warraich et al., 2013). This mouse lacks the gene encoding equilibrative nucleoside transporter 1 (ENT1; solute carrier family 29 member 1; encoded by the gene *Scl29a1*). ENT1 mediates the transport of nucleosides (e.g., adenosine) bi-directionally across the plasma membrane in a sodium-independent manner (Baldwin et al., 2004). With advancing age, the spine of *ENT1*$^{-/-}$ mice resembles that of humans with DISH (Fournier et al., 2019, 2020). Serum calcium and phosphate levels are comparable in *ENT1*$^{-/-}$ and wild-type mice (Warraich et al., 2013), arguing against the possibility that lesions arise due to metastatic calcification. In both the mouse model and humans with DISH, lesions are non-inflammatory (Warraich et al., 2013; Fournier et al., 2020). However, it is unknown which tissue is the site of initiation of ectopic calcification. In the present study, we explored the orofacial region of mice lacking ENT1 because of the diversity of connective tissue types in this region.

The orofacial region encompasses of a plethora of mineralised and nonmineralised connective tissues and structures (e.g., bone, dentin, cementum, ligaments, symphyses, articular joints, lamina propria, dermis, etc.) which, if affected in this mouse model, could provide insight into the early pathogenesis of ectopic calcification. Pathological mineral formation is known to occur in orofacial tissues and such disorders include pulp stones, hypercementosis, sialolithiasis, and myositis ossificans traumatica of the masticatory muscles (Goga et al., 2008; Hanisch et al., 2018; Kraaij et al., 2014; Weinberger, 1954). Heterotopic ossification can also affect the temporomandibular joint following surgery or trauma (Mercuri and Saltzman, 2017). Clinical features of ectopic mineralisation of orofacial structures can include pain, swelling, compression of neural tissue, and restricted mandibular mobility and function.

The causes and biological pathways associated with ectopic mineralisation in humans are poorly understood. As opposed to the spinal tissues in the mouse, the orofacial region encompasses various connective tissues in anatomically well-defined locations, and thus may provide better insights into the processes underlying ectopic mineralisation. The objective of the current study was to investigate the possibility of aberrant calcification of orofacial structures in *ENT1*$^{-/-}$ mice to better understand the pathophysiology of ectopic mineralisation.

2. Materials and methods

2.1. Animals

All aspects of this study were conducted in accordance with the policies and guidelines set forth by the Canadian Council on Animal Care and were approved by the Animal Use Subcommittee of the University of Western Ontario, London, CAN (Protocol No. 2017-154). A completed ARRIVE guidelines checklist (Percie du Sert et al., 2020) is available as Tables S1 and S2. Mice (*Mus musculus*) lacking the gene *Slc29a1* that encodes ENT1 were originally provided by Dr. Doo-Sup Choi, Mayo Clinic College of Medicine and Science, Rochester, MN (Choi et al., 2004). The colony was established by backcrossing mice lacking ENT1 (B6.129X1-*Slc29a1*^{tm1Msg}) with inbred C57BL/6NCrl mice (Charles River, Wilmington, MA). Heterozygotes (*ENT1*$^{+/-}$) were bred to generate wild-type (*ENT1*$^{+/+}$) and knockout (*ENT1*$^{-/-}$) littermates. Genotyping was performed as described previously (Bone et al., 2010).

Mice were housed in standard polycarbonate cages (RC71D-PC, Alternative Design Manufacturing & Supply, Siloam Springs, AR) with natural absorbing and odor control bedding (Bed-o'Cobs® 1/8″ & 1/4″ combination, Andersons Lab Bedding, Maumee, OH) and environmental enrichment (Mouse House, Techniplast, West Chester, PA; and Nestlets, Ancare, Bellmore, NY). Mice experienced a controlled environment with temperature ranging from 22 to 25 °C, relative humidity ranging from 40 to 60%, 12-hour light/dark cycle beginning at 07:00, and ad libitum access to water and a grain-based Teklad Global 18% Protein Rodent Diet (Item No. 2018, Envigo, Madison, WI). Mice were housed with up to three same-sex littermates, bedding was changed weekly, and animal welfare was assessed daily. Mice were euthanized using an intraperitoneal injection of 50 mg/kg of pentobarbital sodium (Item No. 1EUF001, Bimeda, Cambridge, CAN). The heads of wild-type and *ENT1*$^{-/-}$ mice were then removed and, in most cases, fixed in 4% paraformaldehyde for 24 h. Tissues used for physical analyses were not fixed. Mice in this study were 3 to 17 months-of-age, a range over which we have shown previously there is progressive ectopic calcification of spinal tissues in *ENT1*$^{-/-}$ mice (Warraich et al., 2013). Beyond 10 months-of-age, *ENT1*$^{-/-}$ mice demonstrate hind limb dysfunction and paralysis due to extensive spinal calcifications. To reduce these adverse events, the majority of experiments involved mice at 3 and 6 months-of-age. Both male and female mice were studied.

2.2. Microcomputed tomography (μCT)

Heads were embedded in 1% agar and scanned using a conebeam X-ray μCT imaging system (eXplore Locus SP/MS-8, GE Healthcare, London, CAN). The scanner was operated at a peak tube potential of 80 kVp, tube current of 80 mA, and integration time of 3000 ms. Each of the 900 X-ray projections were averaged over four frames to improve signal-to-noise characteristics as the sample rotated 360°. The acquisitions were reconstructed into independent three-dimensional image volumes with isotropic voxel spacing of 11.4 μm using a Feldkamp filtered back-projection algorithm (Feldkamp et al., 1984). Included in the scans was a calibrator consisting of air, water, and a cortical bone-mimicking epoxy (450-SB3, Gammex Inc., Middleton, WI). The final image volumes were scaled into Hounsfield units (HU) based on the average greyscale values of air and water, −1000 and 0 HU, respectively. Imaging data were analysed with MicroView (Version 2.5.0, Parallax Innovations Inc., Ilderton, CAN) and VGStudio MAX (Version 2.0.4, Volume Graphics GmbH, Heidelberg, DEU).

To standardise morphometric analyses, three-dimensional image volumes were oriented with the frontal anatomical plane parallel and the transverse anatomical plane perpendicular to the occlusal plane created by the mandibular molars. Window and level values were set to 8000 and 4000 HU, respectively. We used the following procedure to identify regions of interest (ROIs) within the mandibular symphysis for quantitative analyses of ectopic lesions. ROIs were centred on the midsagittal plane and extended laterally a total of 0.25 mm (~22 multiplanar reformatted sections of μCT data) to avoid including adjacent cortical bone (Fig. S1). The borders of the ectopic lesions in the anterior-posterior and superior-inferior directions were defined by the extent of material with radiodensities $\geq$ 2157 HU (the calculated upper limit for the radiodensity of soft tissues).

Spacing between the hemimandibles was determined as the distance between the lateral cementoenamel junctions of each incisor, measured at four positions in the transverse anatomical plane—position 1, representing the anterior extent of the alveolar bone around the mandibular incisor; and positions 2 to 4 representing 1, 2, and 3 mm posterior from position 1, respectively. Several cephalometric parameters of skulls and mandibles were also assessed. Skull length was measured as the distance between the anterior-most point of the nasal bone and the posterior-most point of the occipital crest. Skull width was measured as the distance between the lateral-most aspect of each zygomatic arch. Mandibular length was measured as the distance between the anterior-most point of alveolar bone around the mandibular incisor and the posterior-most aspect of the condylar process. Mandibular height was measured as the distance between the superior-most point of the coronoid process and the inferior-most aspect of the angular process.

2.3. Histology

Following imaging, the heads of 12 age-matched wild-type and *ENT1*$^{-/-}$ mice at 3 and 6 months-of-age (n = 3 mice per genotype per age) were decalcified with Shandon™ TBD-2 decalcifier (Thermo Fisher Scientific, Waltham, MA) for 4 days. Heads were then embedded in paraffin for serial sectioning (5 μm thick slices) in the transverse anatomical plane RM2255 Rotary Microtome (Leica Biosystems Nußloch GmbH, Nußloch, DEU). Sections of the mandibular symphysis from wild-type and *ENT1*$^{-/-}$ mice were stained by haematoxylin and eosin (H&E) or Lillie's modified trichrome. Light micrographs were acquired using a Leica DM1000 LED microscope, Leica DFC295 digital colour camera, and Leica Application Suite software (Version 3.8.0, Leica Microsystems GmbH, Wetzlar, DEU). One of the authors (PKK) with specialized training in veterinary anatomic pathology, reviewed the stained sections and documented histological features of the mandibular symphysis in wild-type and *ENT1*$^{-/-}$ mice.

2.4. Physical analyses

Mandibles were isolated from heads of wild-type and *ENT1*$^{-/-}$ mice at 8 to 9 months-of-age and associated soft tissues were removed. Mandibles were then desiccated with drying agent for 2 to 4 weeks (Drierite, W.A. Hammond Drierite Co., Xenia, OH). Following drying, these intact mandibles were bisected in the midsagittal plane through the mandibular symphysis (and, when present, the associated ectopic lesion). Representative hemimandibles from age-matched wild-type and *ENT1*$^{-/-}$ mice were selected for physical analyses.

For scanning electron microscopy, the desiccated hemimandibles were coated with a 10 nm layer of osmium, as described (Costa et al., 2012). Scanning electron microscopy images were acquired using a LEO 1540XB FIB/SEM instrument (Carl Zeiss, Oberkochen, DEU) with an electron backscatter detector operated at 15 to 30 kVp at the Nanofabrication Facility, University of Western Ontario, London, CAN. Energy-dispersive X-ray spectra were acquired from selected regions of unaffected cortical bone in the mandibles of wild-type and *ENT1*$^{-/-}$ mice, and regions of ectopic mineral in the symphyses of *ENT1*$^{-/-}$ mice (2 to 8 regions per tissue of interest). Elemental analyses were performed using Integrated Calibration and Application software (INCA, Oxford Instruments, Abingdon, UK) and data were presented as atomic percentage.

Using the same hemimandible tissues, micro X-ray diffraction patterns were collected from regions of unaffected cortical bone in wild-type and *ENT1*$^{-/-}$ mice and regions of ectopic mineral in *ENT1*$^{-/-}$ mice using a Bruker D8 Discover diffractometer (Bruker Co., Billerica, MA) and Bruker-AXS general area detector diffraction system (Bruker AXS GmbH, Karlsruhe, DEU), as described (Flemming, 2007). Samples were mounted on an *XYZ* stage and viewed with an optical microscope and laser system for precise positioning of target locations (1 to 3 regions per tissue of interest). Resultant X-ray diffraction data were analysed with Bruker's DiffracPlus™ EVA software (Bruker Co.).

2.5. Statistics

Statistical analyses were performed using GraphPad Prism (Version 8.01: San Diego, CA). Due to the marked phenotypic difference between *ENT1*$^{-/-}$ and wild-type mice, it was not possible to perform a blinded assessment of μCT or histological images. Data were tested for normality using Shapiro-Wilk's test and for outliers using Grubbs' two-sided test. μCT data were analysed using two-way-ANOVA with Sidak's multiple comparisons test. Elemental data were analysed using parametric, one-way-ANOVA and Sidak's multiple comparisons test. A P value < 0.05 was considered significant.

3. Results

3.1. Ectopic mineralisation of the mandibular symphysis in *ENT1*$^{-/-}$ mice revealed by μCT imaging

μCT was used to identify possible ectopic mineralisation of orofacial tissues. No ectopic mineral was found to be associated with the skin, mucosa, enamel, dentin, cementum, or temporomandibular joint, or within the pulp chamber or periodontal ligament space of wild-type or *ENT1*$^{-/-}$ mice at any age examined (up to 17 months of age). Ectopic radiopaque material was however identified in the mandibular symphysis of *ENT1*$^{-/-}$ mice. Radiopaque lesions were not observed in age-matched wild-type mice (Fig. 1A and B) and were most pronounced in both male and female *ENT1*$^{-/-}$ mice at advanced ages (Figs. 1A and C, 2A). In contrast to the mandibular symphysis, no ectopic mineral was found associated with sutures or synchondroses in the skulls of *ENT1*$^{-/-}$ mice. Moreover, cephalometric parameters were similar between wild-type and *ENT1*$^{-/-}$ mice (Fig. S2).

At 3 months of age, ectopic lesions were detected in the mandibular symphysis in 5 of 6 *ENT1*$^{-/-}$ mice as small radiopaque accumulations within an otherwise radiolucent tissue (ectopic mineral is pseudocoloured red in Fig. 2A). Of note, ectopic lesions enlarged with age in all directions within the symphysis and eventually extended beyond the symphysis in the superior direction. At 6 months, all *ENT1*$^{-/-}$ mice showed ectopic lesions within the mandibular symphysis.

Radiographically, lesions were composed of mineralised and non-mineralised material. The volume of lesions was assessed as follows. We created standardised regions of interest (ROIs, 0.25 mm in the medial-lateral direction) centred on the midsagittal plane and confined based on the extent of radiopaque material in the superior-inferior and anterior-posterior directions (Fig. S1). The volume of these ROIs (representing the lesion volumes) differed significantly between genotypes at each age: 3 months (wild-type = 0.001 ± 0.001 mm^3, *ENT1*$^{-/-}$ = 0.010 ± 0.011 mm^3); 6 months (wild-type = 0.003 ± 0.002 mm^3, *ENT1*$^{-/-}$ = 0.546 ± 0.114 mm^3); and 10+ months (wild-type = 0.021 ± 0.018 mm^3, *ENT1*$^{-/-}$ = 1.410 ± 0.157 mm^3). Moreover, there was a significant increase in lesion volume with age in *ENT1*$^{-/-}$ mice.

We next assessed the distribution of radiodensities within the ROIs defined above. To distinguish mineralised and nonmineralised tissue, we established a threshold of 2157 Hounsfield units (HU, four standard deviations above the mean peak radiodensity of known regions of nonmineralised tissue, n = 16 mice). At 3 months, there was little mineralised tissue evident in *ENT1*$^{-/-}$ mice (Fig. 2B). With increasing age, the distribution of radiodensities within the ROIs shifted towards higher HU, indicating a greater proportion of the lesions consisted of mineralised tissue (Fig. 2B).

Because of the severity of ectopic lesions in the mandibular symphysis, we considered the possibility that the hemimandibles were displaced by the lesion in *ENT1*$^{-/-}$ mice. Therefore, we quantified the spacing between hemimandibles in wild-type and *ENT1*$^{-/-}$ mice as the distance between each incisor, measured at four positions in the transverse anatomical plane (Fig. 2C1). There were no significant differences between genotypes in spacing at 3 or 6 months (Fig. 2C2). Whereas, at 10+ months, spacing was slightly less in *ENT1*$^{-/-}$ mice compared to wild-type mice (Fig. 2C2).

3.2. Histological features of the mandibular symphysis at 3 months of age

We next assessed histologic features of the mandibular symphysis in wild-type and *ENT1*$^{-/-}$ mice at 3 months, the age at which *ENT1*$^{-/-}$ mice begin to exhibit lesions. We first assessed transverse μCT sections through the symphysis between positions 1 and 3 in the anterior-posterior direction (as defined in Fig. 2C1). Minimal radiopacities were evident in the symphysis region of wild-type mice (Fig. 3A). H&E (Fig. 3B) and Lillie's trichrome (Fig. 3C) staining of corresponding histological sections from the same wild-type animal shown in Fig. 3A

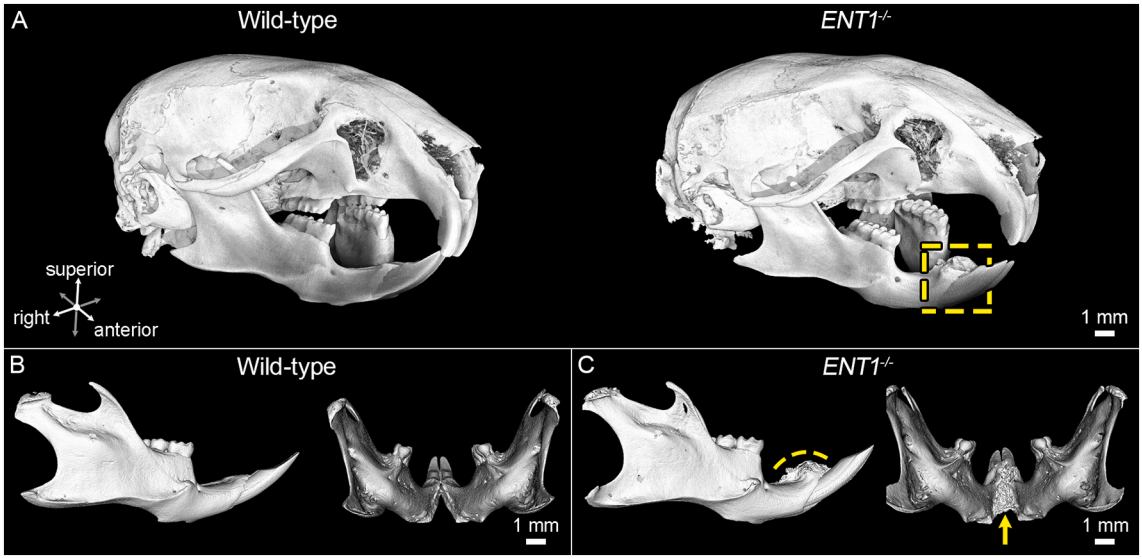

Fig. 1. Representative μCT image renderings of wild-type and *ENT1*$^{-/-}$ mice at 17 months, displaying mineralised material (>2157 HU). (A) Anterolateral view of three-dimensional renderings of intact heads of a wild-type (left) and an *ENT1*$^{-/-}$ (right) mouse. Yellow dashed region highlights extensive ectopic lesion localised to the mandibular symphysis region. (B) Isosurface rendering of an isolated mandible (lateral and posterior views) from the same wild-type mouse shown in panel A. Note the lack of ectopic lesion associated with the mandibular symphysis. (C) Isosurface rendering of an isolated mandible (lateral and posterior views) from the same *ENT1*$^{-/-}$ mouse shown in panel A. Note the extensive ectopic lesion highlighted by yellow dashed line and yellow arrow. Scale bars represent 1 mm. μCT images are representative of 2 mice of each genotype.

revealed the expected structural features of the symphysis. The fibrocartilage pad, which resists compression of the joint (Beecher, 1977, 1979), was evident superiorly where the symphysis is narrowest. The fibrocartilage pad was clearly stained light aqua with Lillie's trichrome, as expected for a collagen-rich tissue. This pad was richly populated by chondrocyte-like cells and was avascular and aneural. Laterally, the fibrocartilage pad anchored into lamellar bone via a chondroid transition zone, which stained slightly more basophilic than the pad with H&E (Fig. 3B1 and B2) and paler with trichrome (Fig. 3C1 and C2). The demarcation between fibrocartilage and chondroid is particularly evident with trichrome (red line in Fig. 3C2, which may represent the tidemark between calcified and noncalcified cartilage). Inferior to the fibrocartilage pad, cruciate ligaments were present (Fig. 3B and C), which resist tensile and shearing forces on the symphysis (Beecher, 1977, 1979). Each ligament was made up of organised bundles of collagen and populated by fibroblasts, with distinct ligaments showing different orientation of fibres. Interspersed among the ligaments were large blood vessels (Fig. 3B and C). Larger histological images of wild-type mice at 3 months are supplied in Fig. S3.

In 3-month-old *ENT1*$^{-/-}$ mice, transverse μCT sections through the symphysis revealed only a small localised deposit of radiopaque material (Fig. 3D, outlined by yellow dashes, representative of 5 of 6 mice examined). The cortical bone lateral to the symphysis in 3-month-old mice appeared intact. Corresponding histological sections from the same *ENT1*$^{-/-}$ mouse revealed features associated with lesion development. At 3 months, the lesion clearly involved a portion of the fibrocartilage pad, without including the cruciate ligaments or blood vessels (Fig. 3E and F). Between the ectopic lesion and the cruciate ligaments, there was a band of densely arranged spindle-shaped cells (Fig. 3E4 and F4).

Higher magnification views revealed that these lesions exhibited regions of eosinophilic granular material with decreased cellularity and loss of aqua staining with trichrome (Fig. 3E1–3 and F1–3). Regions of remaining fibrocartilage appeared disorganised with cells in less well-defined lacunae. Larger histological images of the mandibular symphysis from *ENT1*$^{-/-}$ mice at 3 months are supplied in Figs. S4 and S5.

3.3. Histological features of the mandibular symphysis at 6 months of age

In wild-type mice, the histological appearance of the symphysis at 6 months (Fig. 4A, larger image supplied in Fig. S6) was essentially the same as its appearance at 3 months (Fig. 3A). In 6-month-old *ENT1*$^{-/-}$ mice, transverse μCT sections through the symphysis revealed extensive ectopic radiopaque material (Fig. 4D, yellow dashed region, representative of 4 of 4 mice examined). As well, the surface of the cortical bone lateral to the symphysis appeared to be eroded, in contrast to its appearance at 3 months-of-age. Corresponding histological sections from the same *ENT1*$^{-/-}$ mouse revealed marked disruption of structural organisation in the mid-region of the symphysis (Fig. 4E and F), matching the distribution of radiopaque material. The lesion appeared to involve much of the fibrocartilage pad, resulting in disorganisation and decreased cellularity (Fig. 4E1). As well, there was loss of aqua staining with Lillie's trichrome, consistent with decreased collagen content, although remnants of the fibrocartilage pad persisted superior to the lesion (Fig. 4F1). Higher magnification views revealed regions of granular material containing eosinophilic cell outlines within the ectopic lesion (Fig. 4E2 and F2). Further inferiorly, there were regions of acellular amorphous material. This material was eosinophilic with H&E and red with trichrome, with paler staining towards the centre of the amorphous material (Fig. 4E3, 4 and F3, 4). It is likely that the amorphous and possibly granular regions are the areas of ectopic calcification which, together with the surrounding loose stroma-like tissue (stained poorly for collagen, Fig. 4F4), have replaced both the inferior aspect of the fibrocartilage pad and the superior aspect of the cruciate ligaments. Moreover, blood vessels were less prominent in these regions than in wild-type mice. Inferiorly, between the ectopic lesion and the remaining cruciate ligaments was a band of densely arranged spindle-shaped cells (Fig. 4E5, 6 and F5, 6) that was also noted in 3-month-old *ENT1*$^{-/-}$ mice. In contrast to the lesion immediately superior, cells within this band appeared viable and proliferative. These cells were basophilic when stained with H&E, stained intensely red with trichrome, and were associated with little if any extracellular matrix.

In *ENT1*$^{-/-}$ mice at 6 months, the eroded appearance of the bone surface at the lateral borders of the symphysis, along with the lack of displacement of the hemimandibles, suggested that bone was resorbed

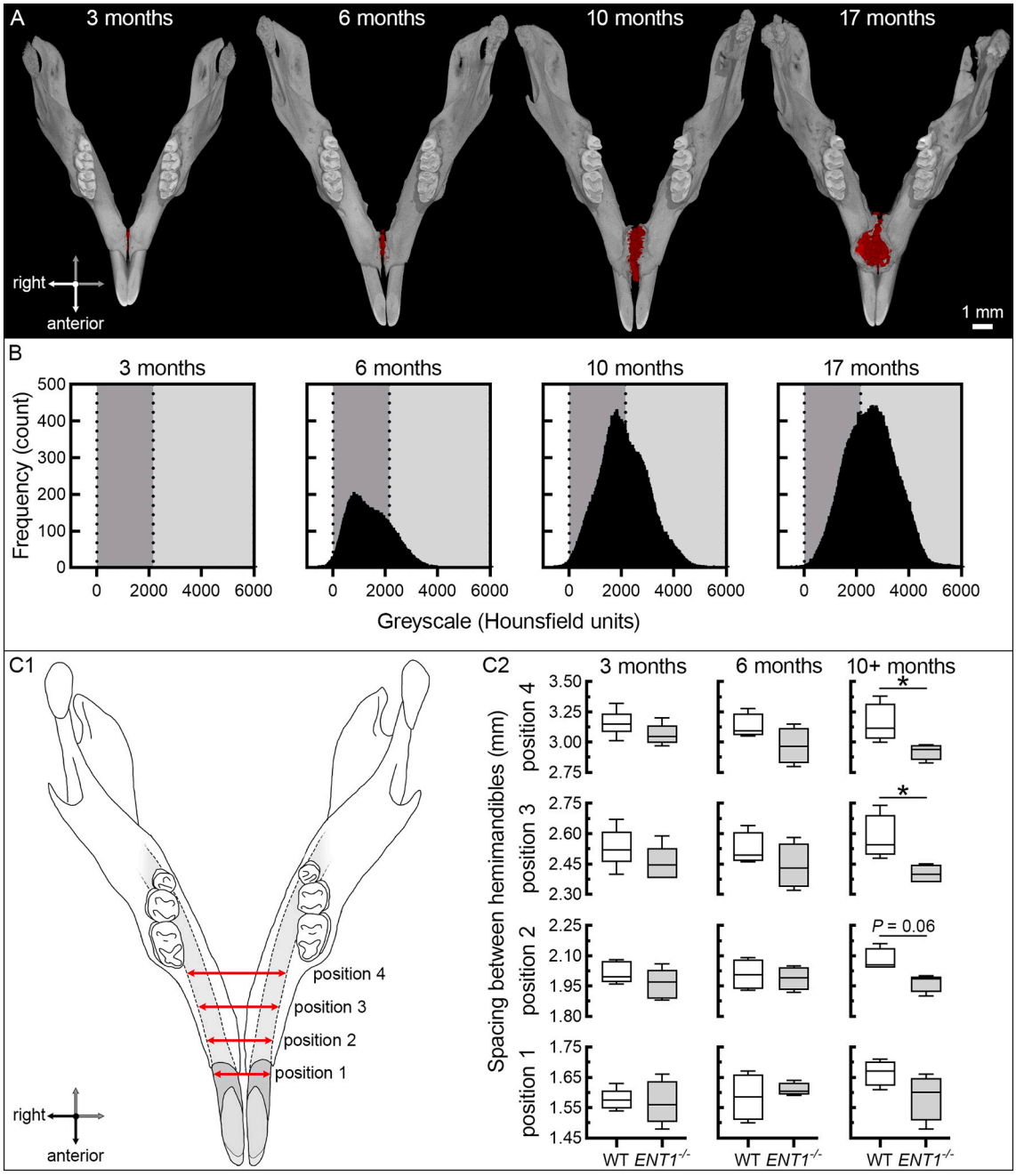

Fig. 2. µCT analyses of the mandibles of wild-type and *ENT1*$^{-/-}$ mice. (A) Representative three-dimensional renderings (superior view) of isolated mandibles from *ENT1*$^{-/-}$ mice at 3, 6, 10, and 17 months. To display the spatiotemporal progression of ectopic lesion of the mandibular symphysis region, mineralised material (>2157 HU) is pseudocoloured red. Scale bar represents 1 mm. (B) Histograms of the frequency distribution of radiodensities of the voxels within the ectopic lesions in *ENT1*$^{-/-}$ mice at the indicated ages. For this analysis, we established standardised ROIs (0.25 mm in the medial-lateral direction) containing both mineralised and nonmineralised material, which were centred on the midsagittal plane and confined based on the extent of radiopaque material (as illustrated in detail in Fig. S1). The range of radiodensities for nonmineralised tissues was 0 to 2157 HU (shaded dark grey) and for mineralised tissue was >2157 HU (shaded light grey). Data are means from 6 mice for 3 months, 4 mice for 6 months, and 2 mice each for 10 and 17 months. (C1) The spacing between hemimandibles was measured as the distance between the lateral cementoenamel junctions of each incisor. Distances were measured at four positions in the transverse anatomical plane, starting at the anterior most crest of cortical bone around the incisor (position 1) and then at 1 mm intervals posteriorly (positions 2 to 4). (C2) Hemimandible spacing data are displayed as box-and-whisker plots; WT, wild-type (white boxes) and *ENT1*$^{-/-}$ (grey boxes). Data are medians with boxes representing the interquartile range and whiskers representing the maximum and minimum values, n = 6 mice for 3 months, n = 4 mice each for 6 and 10+ months (10 and 17 months combined) for each genotype. * represents significant differences between genotypes assessed using two-way-ANOVA with Sidak's multiple comparisons test (*P* value < 0.05).

as the ectopic lesions expanded. In this regard, osteoclasts were observed where the ectopic lesion interfaced with bone (e.g. Fig. 4E3 inset). Furthermore, multiple lacunae were evident on the bone margins indicative of previous osteoclast activity. Notably, there was a lack of inflammatory or phagocytic cells throughout the mandibular symphysis of *ENT1*$^{-/-}$ mice. Larger histological images of *ENT1*$^{-/-}$ mice at 6 months are supplied in Figs. S7 and S8.

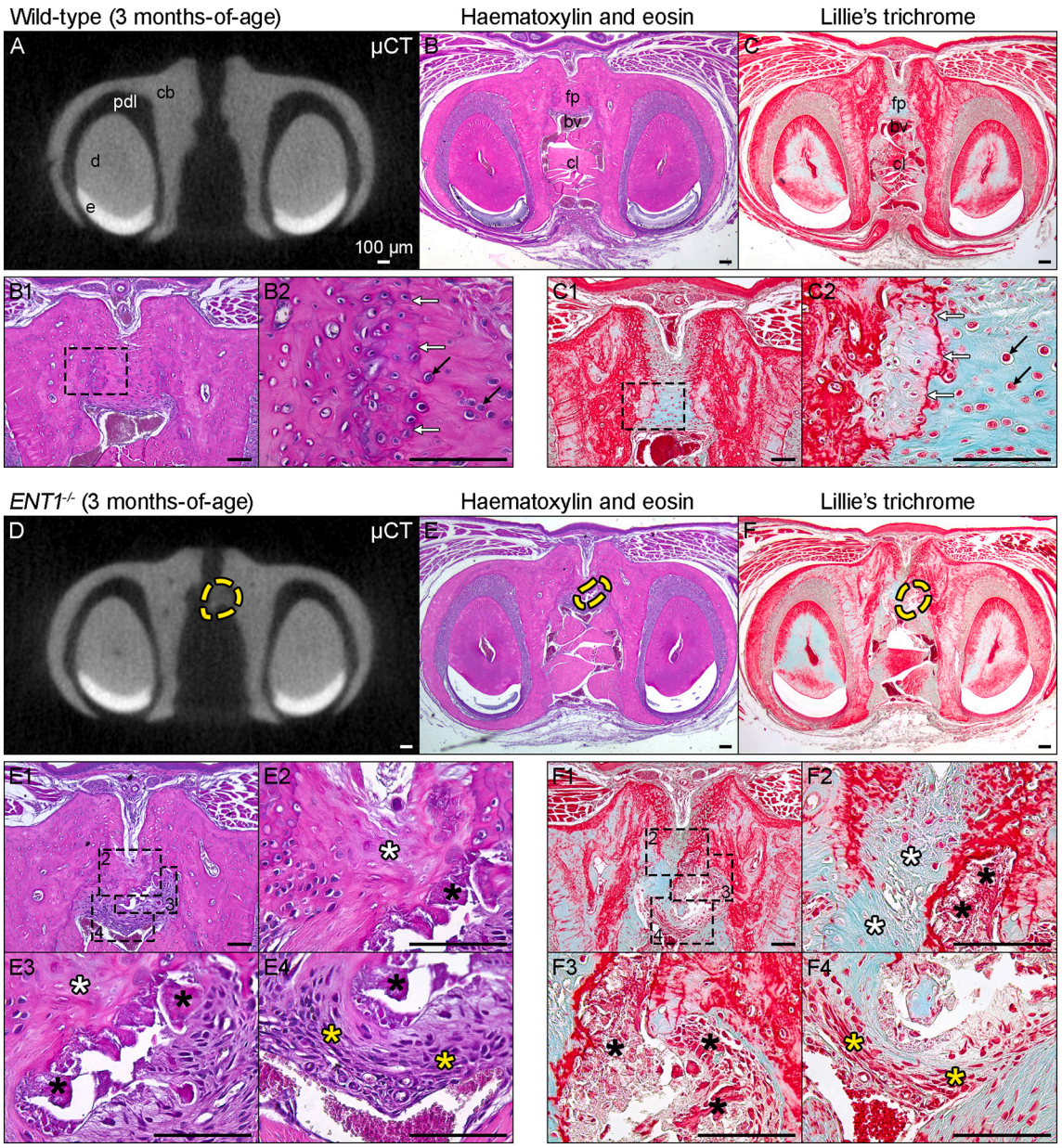

Fig. 3. Histological appearance of the mandibular symphysis from a representative wild-type and *ENT1*$^{-/-}$ mouse at 3 months. (A) Single transverse section of μCT image volume from the mid-symphysis region of a wild-type mouse. Thickness of μCT section is 11.4 μm. Scale bars in all panels represent 100 μm: cb, cortical bone; e, enamel; d, dentin; and pdl, periodontal ligament space. (B and C) Tissues from the same wild-type mouse as in panel A were decalcified, sectioned, and stained with haematoxylin and eosin or Lillie's trichrome. Transverse sections were matched to the μCT image in the anterior-posterior axis and display the general features of the wild-type mandibular symphysis: bv, blood vessel; cl, cruciate ligaments; and fp, fibrocartilage pad. (B1 and C1) Higher magnification images of the superior aspect of the symphysis. Dashed rectangles show regions displayed at even higher power in B2 and C2. Chondrocyte-like cells of the fibrocartilage pad are highlighted by black arrows, and the demarcation between fibrocartilage and chondroid material is highlighted by white arrows. (D) Single transverse section of μCT image volume from the mid-symphysis region of an *ENT1*$^{-/-}$ mouse. Thickness of μCT section is 11.4 μm. Ectopic lesion is indicated by yellow dashed lines. Scale bar represents 100 μm. (E and F) Tissues from the same *ENT1*$^{-/-}$ mouse as in panel D were decalcified, sectioned, and stained with haematoxylin and eosin or Lillie's trichrome. Transverse sections were matched to the μCT image in the anterior-posterior axis. Note the disruption of the fibrocartilage pad and the presence of ectopic lesion (indicated by yellow dashed lines). (E1 and F1) Higher magnification images of the superior aspect of the symphysis. Dashed rectangles show regions displayed at even higher power in E2–4 and F2–4, illustrating the fibrocartilage pad (E2 and F2), ectopic lesion (E3 and F3), and inferior aspect of the mandibular symphysis (E4 and F4). Ectopic lesions were characterised by granular material (black asterisks) and decreased cellularity of the fibrocartilage pad (white asterisks). Inferiorly, densely arranged spindle-shaped cells are shown (yellow asterisks). μCT images are representative of 4 mice of each genotype. Histological images are representative of 12 sections from at least 3 mice of each genotype.

3.4. Elemental composition and X-ray diffraction of mineralised tissues

We examined age-matched mandibles from wild-type and *ENT1*$^{-/-}$ mice (8 to 9 months). Desiccated mandibles were bisected in the midsagittal plane through the symphysis, exposing lesion material in *ENT1*$^{-/-}$ mice. Unaffected cortical bone was examined in both genotypes and ectopic lesions were assessed in *ENT1*$^{-/-}$ mice. Images of the symphysis region were obtained by scanning electron microscopy (Fig. 5A1, left panel from an *ENT1*$^{-/-}$ mouse; orientation is shown in Fig. S9). Energy-dispersive X-ray spectroscopy provided elemental mapping of the region (e.g., Fig. 5A1, right panels). ROIs were then selected for quantification based on the elemental maps and surface

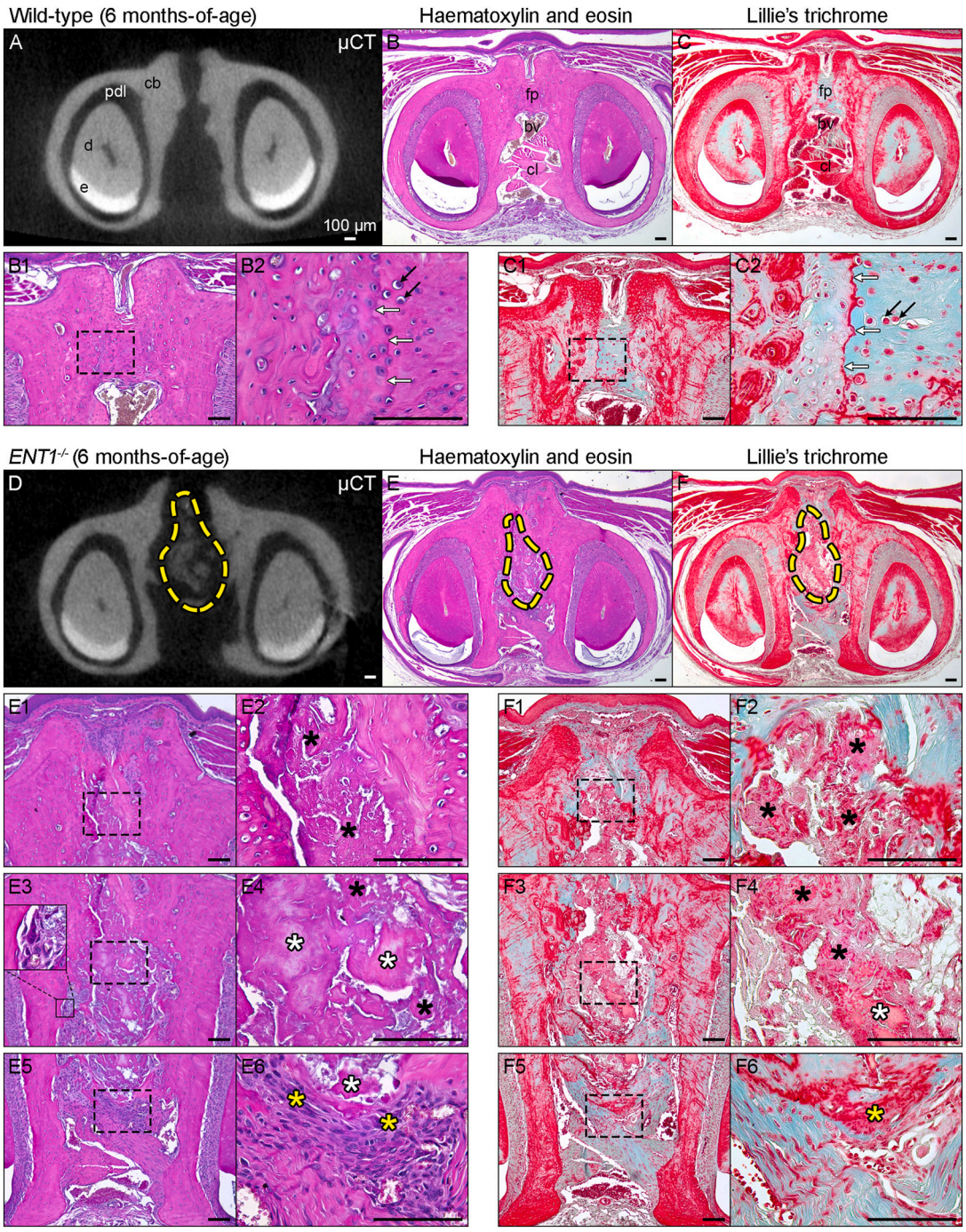

Fig. 4. Histological appearance of the mandibular symphysis from a representative wild-type and *ENT1*$^{-/-}$ mouse at 6 months. (A) Single transverse section of µCT image volume from the mid-symphysis region of a wild-type mouse. Thickness of µCT section is 11.4 µm. Scale bars in all panels represent 100 µm: cb, cortical bone; e, enamel; d, dentin; and pdl, periodontal ligament space. (B and C) Tissues from the same wild-type mouse as in panel A were decalcified, sectioned, and stained with haematoxylin and eosin or Lillie's trichrome. Transverse sections were matched to the µCT image in the anterior-posterior axis and display the general features of the wild-type mandibular symphysis: bv, blood vessel; cl, cruciate ligaments; and fp, fibrocartilage pad. (B1 and C1) Higher magnification images of the superior aspect of the symphysis. Dashed rectangles show regions displayed at even higher power in B2 and C2. Chondrocyte-like cells of the fibrocartilage pad are highlighted by black arrows, and the demarcation between fibrocartilage and chondroid material is highlighted by white arrows. (D) Single transverse section of µCT image volume from the mid-symphysis region of an *ENT1*$^{-/-}$ mouse. Thickness of µCT section is 11.4 µm. Ectopic lesion is indicated by yellow dashed lines. (E and F) Tissues from the same *ENT1*$^{-/-}$ mouse as in panel D were decalcified, sectioned, and stained with haematoxylin and eosin or Lillie's trichrome. Transverse sections were matched to the µCT image in the anterior-posterior axis. Note the disruption of the structural features of the mandibular symphysis and the extensive ectopic lesion (indicated by yellow dashed lines). Higher magnification images of the mandibular symphysis: superior (E1 and F1), middle (E3 and F3), and inferior (E5 and F5) aspects. Dashed rectangles show regions displayed at even higher power in E2, 4, 6 and F2, 4, 6. Ectopic lesions were characterised by granular (black asterisks) and acellular material (white asterisks). Inferiorly, densely arranged spindle-shaped cells are shown (yellow asterisks). Inset in E3 displays an osteoclast where the ectopic lesion interfaced with bone. µCT images are representative of 4 mice of each genotype. Histological images are representative of 12 sections from at least 3 mice of each genotype.

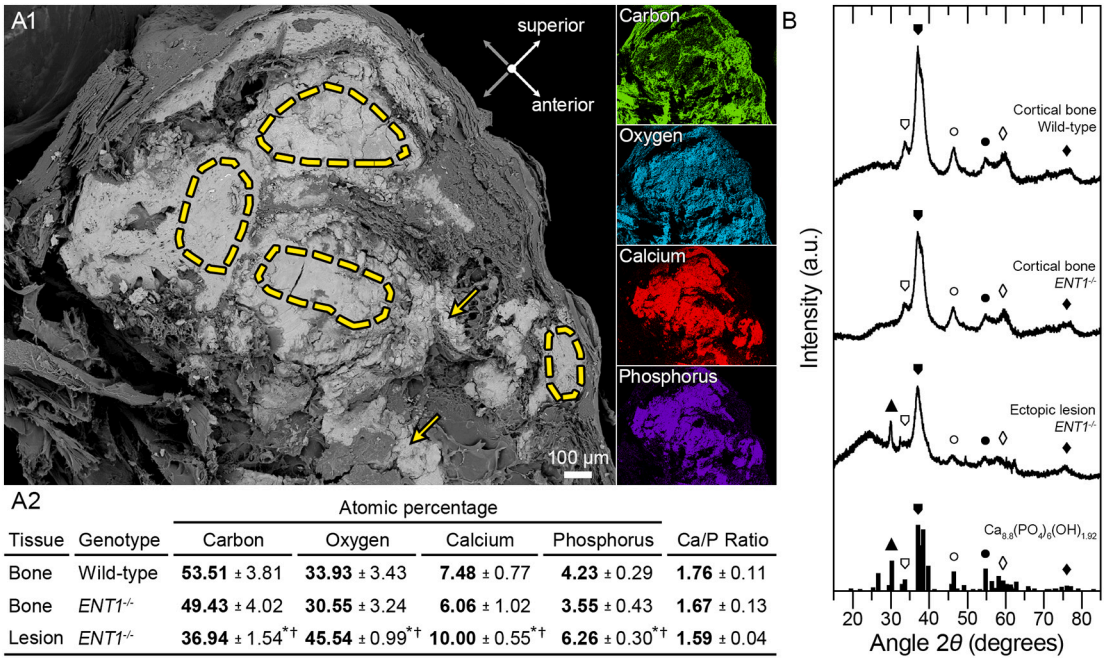

A2

		Atomic percentage				
Tissue	Genotype	Carbon	Oxygen	Calcium	Phosphorus	Ca/P Ratio
Bone	Wild-type	**53.51** ± 3.81	**33.93** ± 3.43	**7.48** ± 0.77	**4.23** ± 0.29	**1.76** ± 0.11
Bone	*ENT1*$^{-/-}$	**49.43** ± 4.02	**30.55** ± 3.24	**6.06** ± 1.02	**3.55** ± 0.43	**1.67** ± 0.13
Lesion	*ENT1*$^{-/-}$	**36.94** ± 1.54*†	**45.54** ± 0.99*†	**10.00** ± 0.55*†	**6.26** ± 0.30*†	**1.59** ± 0.04

Fig. 5. Physical characterisation of the mandibular symphysis in wild-type and *ENT1*$^{-/-}$ mice at 8 to 9 months. (A1) Scanning electron microscopy image of ectopic lesion in the mandibular symphysis of a representative *ENT1*$^{-/-}$ mouse; scale bar represents 100 µm. Images at right show localisation of carbon (green), oxygen (aqua), calcium (red), and phosphorus (purple) in the same field, as determined by energy-dispersive X-ray spectroscopy. Orientation of the sample is illustrated in Fig. S8. (A2) Atomic percentage data collected from multiple regions of cortical bone in wild-type and *ENT1*$^{-/-}$ mice and from regions of ectopic lesion in *ENT1*$^{-/-}$ mice (n = 5 mice, 2–8 ROI per tissue type). Examples of regions of ectopic lesion analysed for elemental spectra are indicated by yellow dashed lines in panel A. Grubbs' two-sided test (*P* value < 0.05) identified two outliers that were removed (1 ROI from *ENT1*$^{-/-}$ cortical bone and 1 ROI from *ENT1*$^{-/-}$ lesion). Data are means ± standard errors of the mean. * denotes significant differences between *ENT1*$^{-/-}$ ectopic lesion and wild-type cortical bone; and † denotes significance differences between *ENT1*$^{-/-}$ ectopic lesion and *ENT1*$^{-/-}$ cortical bone determined using parametric one-way-ANOVA with Sidak's multiple comparisons test (*P* value < 0.05). There were no significant differences in the elemental composition of cortical bone in wild-type and *ENT1*$^{-/-}$ mice. (B) Representative micro X-ray diffraction patterns of regions of cortical bone from wild-type and *ENT1*$^{-/-}$ mice and regions of ectopic lesion in the mandibular symphysis of *ENT1*$^{-/-}$ mice. Examples of regions used for X-ray diffraction analysis are indicated by yellow arrows in panel A. X-ray diffraction patterns were matched to that of calcium-deficient hydroxyapatite (powder diffraction file: 86-1201, $Ca_{8.8}(PO_4)_6(OH)_{1.92}$ from the International Center for Diffraction Data), plotted as histogram on the x-axis. Corresponding peaks are indicated by matching symbols.

appearance indicative of calcification (e.g., areas enclosed by dashed yellow lines in Fig. 5A1, left panel). There were no significant differences in the elemental composition of mandibular cortical bone in wild-type and *ENT1*$^{-/-}$ mice. Ectopic lesions contained significantly greater percentages of calcium, phosphorus, and oxygen compared to cortical bone (Fig. 5A2). Conversely, the percentage of carbon was less in ectopic lesions than in cortical bone. The resultant calcium/phosphorus ratios were similar for both ectopic lesions and cortical bone. These data are consistent with ectopic lesions being rich in calcium and phosphate, and containing less organic matrix than cortical bone. To identify the nature of the mineral within ectopic lesions, we performed micro X-ray diffraction. Diffraction patterns for both unaffected cortical bone and regions of ectopic lesion closely matched the pattern of calcium-deficient hydroxyapatite (Fig. 5B). These data align with the observed calcium/phosphorus ratios ranging from 1.59 to 1.76.

4. Discussion

4.1. Ectopic lesions in *ENT1*$^{-/-}$ mice

Histological analysis of decalcified samples revealed that, by 6 months, the mandibular symphysis contained large accumulations of amorphous, eosinophilic acellular material with loss of existing structural elements. These lesions clearly do not involve the ectopic bone formation, rather they resemble features reported for ectopic calcifications in the paraspinal ligaments and intervertebral discs of *ENT1*$^{-/-}$ mice (Warraich et al., 2013). Notably, we were able to determine that ectopic lesions in the symphysis initiated in the fibrocartilage pad, without involving the cruciate ligaments at this stage. In previous studies of spinal tissues, we were unable to identify in which tissue ectopic lesions initiated; the reason being that ectopic lesions could only be localised once sufficient mineral had accumulated to enable detection by µCT (Warraich et al., 2013). By this stage, multiple tissues were often involved including the paraspinal ligaments and annulus fibrosus of the intervertebral disc, and the complex anatomy of spinal tissues made it difficult to identify the site of initiation. In contrast, the spatially localised nature of the mandibular symphysis provided an opportunity to characterise the early features and progression of these lesions. The present study showed that lesions originate within the fibrocartilage of the mandibular symphysis, suggesting that fibrocartilaginous tissues may be the sites at which ectopic calcifications arise within spinal tissues as well.

Mineral deposits in both the mandibular symphysis and spinal tissues of *ENT1*$^{-/-}$ mice are composed of similar amounts of calcium and phosphorus, with calcium:phosphorus ratios of approximately 1.6 and 1.5, respectively (Fig. 5A2, Warraich et al., 2013). Moreover, the current study is the first to perform X-ray diffraction analysis of ectopic lesions in *ENT1*$^{-/-}$ mice revealing the presence of calcium-deficient hydroxyapatite. Interestingly, investigation of ectopic mineralisation in humans with DISH also revealed that lesions exhibited regions of dystrophic calcification containing calcium-deficient hydroxyapatite (Fournier et al., 2020). Of note, mineral deposits in the mandibular symphysis contained significantly less carbon and more calcium and phosphorus than mandibular bone. This finding is consistent with a lower proportion of organic matrix in ectopic lesions than in bone.

In contrast to spinal lesions in *ENT1*$^{-/-}$ mice (Warraich et al., 2013),

the distinct spatial localisation of lesions in the mandibular symphysis allowed us to evaluate the interface of the developing ectopic lesion with cortical bone and ligamentous structures. In the current study, osteoclasts and Howship's lacunae were identified where the lesion interfaced with cortical bone. Previous studies of *ENT1*$^{-/-}$ mice demonstrated higher mRNA levels for tartrate-resistant acid phosphatase in the femur of these animals compared to wild-type mice (Hinton et al., 2014), consistent with the possibility of a generalised increase in osteoclast activity. Furthermore, since ectopic lesions do not displace the hemimandibles, resorption of the mandibular margins may arise from sustained pressure due to the lesion expanding in a confined space. In addition to resorption of cortical bone, the cruciate ligaments were destroyed as ectopic lesions progressed with age. It is possible that, as in the symphysis, ectopic lesions originating in the fibrocartilage of spinal tissues progress to involve the paraspinal ligaments.

Interestingly, in the mandibular symphysis, we identified a region of aberrant hypercellularity between the ectopic calcification and the remaining cruciate ligament tissue. This feature was not reported in the spinal tissues of *ENT1*$^{-/-}$ mice (Warraich et al., 2013). On the other hand, studies of the annulus fibrosus of intervertebral discs from *ENT1*$^{-/-}$ mice have revealed enrichment of cell cycle pathways and accumulation of PCNA-positive cells (Veras et al., 2019). It is conceivable that this hypercellular region reflects a localised increase in cell proliferation, which may have given rise to the enrichment of cell cycle pathways reported previously in intervertebral discs. It is also conceivable that this band of fibroblast-like cells reflects reactive fibrosis (Wynn, 2008) in response to the ectopic calcification.

4.2. Possible mechanism underlying ectopic calcification in the mandibular symphysis

In rodents, the fibrocartilage pad of the symphysis resists compression during mandibular function, while the cruciate ligaments resist tensile and shearing forces (Beecher, 1977, 1979). Together, these tissues permit mobility of the hemimandibles to accommodate bilateral mastication and incisor occlusion (Weijs, 1975). Therefore, it is likely that the fibrocartilage pad is exposed to repetitive compression during mandibular function. In this regard, it is known that compression of cartilage leads to the release of ATP from chondrocytes (Corciulo and Cronstein, 2020). Once in the extracellular fluid, ATP is rapidly broken-down releasing adenosine (Haskó et al., 2018). Given the avascular nature of fibrocartilage and the disrupted transport of adenosine in *ENT1*$^{-/-}$ mice, it is conceivable that there is aberrant adenosine accumulation within the fibrocartilage pad of these mice. Increased extracellular adenosine levels could enhance signaling through adenosine receptors present on chondrocytes and many other cell types (Borea et al., 2018; Corciulo and Cronstein, 2020). It is possible that lesions develop in *ENT1*$^{-/-}$ mice specifically at sites (e.g., mandibular symphysis, spinal tissues) where fibrocartilage is frequently subjected to mechanical deformation.

Mice lacking ENT1 have elevated plasma levels of adenosine (Pastor-Anglada and Pérez-Torras, 2018; Warraich et al., 2013). Moreover, it has been shown that expression of mineralisation inhibitors (e.g., *Mgp*, *Enpp1*, *Ank*, and *Spp1*) is suppressed in the annulus fibrosus of *ENT1*$^{-/-}$ mice at 6 months, possibly contributing to ectopic calcification (Ii et al., 2016). These studies also demonstrated that genes associated with chondrocyte hypertrophy (e.g., *Runx2*, *Col10a1*) were not altered in *ENT1*$^{-/-}$ mice. Changes in gene expression (Ii et al., 2016) and increases in cell proliferation (Veras et al., 2019) may arise from increased adenosine signaling in the tissues of *ENT1*$^{-/-}$ mice. Interestingly, a rare mutation in humans that results in loss of function of ENT1 has been linked to ectopic mineralisation (Daniels et al., 2015), further establishing a role for adenosine transport in pathological calcification.

4.3. Comparison of lesions in the symphysis of *ENT1*$^{-/-}$ mice with lesions in human DISH

There are striking similarities in the symphyseal lesions of *ENT1*$^{-/-}$ mice and those in human DISH. In both, the severity of lesions increases with age. In addition, the elemental composition and X-ray diffraction profiles of lesions are comparable (Fig. 5, Fournier et al., 2020). Histologically, indicators of inflammation are absent in both the symphysis of *ENT1*$^{-/-}$ mice and DISH lesions. Specifically, ectopic calcifications in *ENT1*$^{-/-}$ mice resemble dystrophic calcifications reported in humans with DISH (Fournier et al., 2020). However, heterotopic ossification is also described in human DISH (Fournier et al., 2020; Kuperus et al., 2016). It has been proposed that, in DISH, initial dystrophic calcifications subsequently transform into heterotopic ossifications (Fournier et al., 2020). Thus, the *ENT1*$^{-/-}$ mouse may be a preclinical model for the early stages of DISH in humans.

Although the mandibular symphysis fuses early in life in humans (Standring, 2016), the advantage of studying the mandibular symphysis in *ENT1*$^{-/-}$ mice is the localised spatiotemporal development of ectopic lesions in this region. This model may prove useful for testing therapeutic treatments to halt the progression of ectopic calcification. As well, the mandibular symphysis of *ENT1*$^{-/-}$ mice may be a useful system for future mechanistic studies of ectopic calcification.

CRediT authorship contribution statement

Dale E. Fournier: Methodology, Formal analysis, Investigation, Writing – original draft, Writing – review & editing. **Kim L. Beaucage:** Conceptualization, Methodology, Formal analysis, Investigation, Writing – review & editing. **Ryan J. Beach:** Methodology, Formal analysis, Investigation, Writing – review & editing. **Patti K. Kiser:** Investigation, Writing – review & editing. **Cheryle A. Séguin:** Conceptualization, Methodology, Investigation, Resources, Writing – review & editing, Supervision, Project administration, Funding acquisition. **S. Jeffrey Dixon:** Conceptualization, Methodology, Investigation, Resources, Writing – original draft, Writing – review & editing, Supervision, Project administration, Funding acquisition.

Transparency document

The Transparency document associated with this article can be found, in online version.

Declaration of competing interest

The authors declare that they have no known competing financial interests or personal relationships that could have appeared to influence the work reported in this paper.

Acknowledgements

We thank Diana Quinonez for animal breeding, genotyping, and dissections; Western's Animal Care and Veterinarian Services for animal husbandry and care; Sumeeta Warraich for assistance with histology; Caroline O'Neil from Robarts Research Institute's Molecular Pathology Core for assistance with histological processing and trichrome staining; Dr. Justin Tse, Chris Norley and Dr. David Holdsworth (Preclinical Imaging Research Centre, Robarts Research Institute) for assistance with μCT scanning and volume reconstructions; Dr. Roberta Flemming and Alex Rupert (Department of Earth Sciences) for their expertise with micro X-ray diffraction; and Dr. Todd Simpson (Western Nanofabrication Facility) for his expertise with scanning electron microscopy and energy-dispersive X-ray spectroscopy.

Funding sources

This study was supported by the Canadian Institutes of Health Research [Grant No. 115068]. DEF was supported in part by a Transdisciplinary Bone and Joint Training Award from the Collaborative Specialization in Musculoskeletal Health Research (CMHR) at the University of Western Ontario, CAN; and a scholarship from the Arthritis Society [No. 19-0469]. KBL was supported in part by the Schulich Dentistry Research Opportunity Program at the University of Western Ontario. CAS is supported by a Career Development Award from the Arthritis Society. The authors declare no potential conflicts of interest with respect to the authorship and/or publication of this article.

Appendix A. Supplementary data

Supplementary data to this article can be found online at https://doi.org/10.1016/j.bonr.2021.101100.

References

Baldwin, S.A., Beal, P.R., Yao, S.Y., et al., 2004. The equilibrative nucleoside transporter family, slc29. Pflugers Arch. 447, 735–743. https://doi.org/10.1007/s00424-003-1103-2.

Beecher, R.M., 1977. Function and fusion at the mandibular symphysis. Am. J. Phys. Anthropol. 47, 325–335. https://doi.org/10.1002/ajpa.1330470213.

Beecher, R.M., 1979. Functional significance of the mandibular symphysis. J. Morphol. 159, 117–180. https://doi.org/10.1002/jmor.1051590109.

Bone, D.B., Choi, D.-S., Coe, I.R., Hammond, J.R., 2010. Nucleoside/nucleobase transport and metabolism by microvascular endothelial cells isolated from ent1−/− mice. Am. J. Physiol. Heart Circ. Physiol. 299, H847–H856. https://doi.org/10.1152/ajpheart.00018.2010.

Borea, P.A., Gessi, S., Merighi, S., Vincenzi, F., Varani, K., 2018. Pharmacology of adenosine receptors: the state of the art. Physiol. Rev. 98, 1591–1625. https://doi.org/10.1152/physrev.00049.2017.

Choi, D.-S., Cascini, M.-G., Mailliard, W., et al., 2004. The type 1 equilibrative nucleoside transporter regulates ethanol intoxication and preference. Nat. Neurosci. 7, 855–861. https://doi.org/10.1038/nn1288.

Corciulo, C., Cronstein, B.N., 2020. Signaling of the purinergic system in the joint. Front. Pharmacol. 10, 1591. https://doi.org/10.3389/fphar.2019.01591.

Costa, D.O., Allo, B.A., Klassen, R., Hutter, J.L., Dixon, S.J., Rizkalla, A.S., 2012. Control of surface topography in biomimetic calcium phosphate coatings. Langmuir 28, 3871–3880. https://doi.org/10.1021/la203224a.

Daniels, G., Ballif, B.A., Helias, V., et al., 2015. Lack of the nucleoside transporter ent1 results in the Augustine-null blood type and ectopic mineralization. Blood 125, 3651–3654. https://doi.org/10.1182/blood-2015-03-631598.

Feldkamp, L.A., Davis, L., Kress, J.W., 1984. Practical cone-beam algorithm. J. Opt. Soc. Am. A Opt. Image Sci. Vis. 1, 612–619. https://doi.org/10.1364/JOSAA.1.000612.

Flemming, R.L., 2007. Micro x-ray diffraction (μxrd): a versatile technique for characterization of earth and planetary materials. Can. J. Earth Sci. 44, 1333–1346. https://doi.org/10.1139/e07-020.

Forestier, J., Rotes-Querol, J., 1950. Senile ankylosing hyperostosis of the spine. Ann. Rheum. Dis. 9, 321–330. https://doi.org/10.1136/ard.9.4.321.

Fournier, D.E., Norley, C.J.D., Pollmann, S.I., Bailey, C.S., Al Helal, F., Willmore, K.E., et al., 2019. Ectopic spinal calcification associated with diffuse idiopathic skeletal hyperostosis (DISH): a quantitative micro-ct analysis. J. Orthop. Res. 37, 717–726. https://doi.org/10.1002/jor.24247.

Fournier, D.E., Kiser, P.K., Beach, R.J., Dixon, S.J., Séguin, C.A., 2020. Dystrophic calcification and heterotopic ossification in fibrocartilaginous tissues of the spine in diffuse idiopathic skeletal hyperostosis (DISH). Bone Res. 8, 1–10. https://doi.org/10.1038/s41413-020-0091-6.

Giachelli, C., 1999. Ectopic calcification: gathering hard facts about soft tissue mineralization. Am. J. Pathol. 154, 671–675. https://doi.org/10.1016/S0002-9440(10)65313-8.

Goga, R., Chandler, N., Oginni, A., 2008. Pulp stones: a review. Int. Endod. J. 41, 457–468. https://doi.org/10.1111/j.1365-2591.2008.01374.x.

Hanisch, M., Hanisch, L., Fröhlich, L.F., Werkmeister, R., Bohner, L., Kleinheinz, J., 2018. Myositis ossificans traumatica of the masticatory muscles: etiology, diagnosis and treatment. Head Face Med 14, 23. https://doi.org/10.1186/s13005-018-0180-6.

Haskó, G., Antonioli, L., Cronstein, B.N., 2018. Adenosine metabolism, immunity and joint health. Biochem. Pharmacol. 151, 307–313. https://doi.org/10.1016/j.bcp.2018.02.002.

Hinton, D.J., McGee-Lawrence, M.E., Lee, M.R., Kwong, H.K., Westendorf, J.J., Choi, D.-S., 2014. Aberrant bone density in aging mice lacking the adenosine transporter ent1. PLoS One 9, e88818. https://doi.org/10.1371/journal.pone.0088818.

Ii, H., Warraich, S., Tenn, N., Quinonez, D., Holdsworth, D.W., Hammond, J.R., et al., 2016. Disruption of biomineralization pathways in spinal tissues of a mouse model of diffuse idiopathic skeletal hyperostosis. Bone 90, 37–49. https://doi.org/10.1016/j.bone.2016.05.008.

Kraaij, S., Karagozoglu, K., Forouzanfar, T., Veerman, E., Brand, H., 2014. Salivary stones: symptoms, aetiology, biochemical composition and treatment. Br. Dent. J. 217, E23. https://doi.org/10.1038/sj.bdj.2014.1054.

Kuperus, J.S., Westerveld, L.A., Rutges, J.P., Alblas, J., van Rijen, M.H., Bleys, R.L., et al., 2016. Histological characteristics of diffuse idiopathic skeletal hyperostosis. J. Orthop. Res. 35, 140–146. https://doi.org/10.1002/jor.23267.

Li, Q., Jiang, Q., Uitto, J., 2014. Ectopic mineralization disorders of the extracellular matrix of connective tissue: molecular genetics and pathomechanisms of aberrant calcification. Matrix Biol. 33, 23–28. https://doi.org/10.1016/j.matbio.2013.06.003.

Mader, R., Verlaan, J.-J., Buskila, D., 2013. Diffuse idiopathic skeletal hyperostosis: clinical features and pathogenic mechanisms. Nat. Rev. Rheumatol. 9, 741–750. https://doi.org/10.1038/nrrheum.2013.165.

Mercuri, L., Saltzman, B., 2017. Acquired heterotopic ossification of the temporomandibular joint. Int. J. Oral Maxillofac. Surg. 46, 1562–1568. https://doi.org/10.1016/j.ijom.2017.06.016.

Pastor-Anglada, M., Pérez-Torras, S., 2018. Who is who in adenosine transport. Front. Pharmacol. 9, 627. https://doi.org/10.3389/fphar.2018.00627.

Percie du Sert, N., Hurst, V., Ahluwalia, A., Alam, S., Avey, M.T., Baker, M., et al., 2020. The ARRIVE guidelines 2.0: updated guidelines for reporting animal research. PLoS Biol. 18, e3000410 https://doi.org/10.1371/journal.pbio.3000410.

Resnick, D., Niwayama, G., 1976. Radiographic and pathologic features of spinal involvement in diffuse idiopathic skeletal hyperostosis (DISH). Radiology 119, 559–568. https://doi.org/10.1148/119.3.559.

Standring, S., 2016. Gray's Anatomy. United Kingdom, Amsterdam.

Veras, M.A., Tenn, N.A., Kuljanin, M., Lajoie, G.A., Hammond, J.R., Dixon, S.J., et al., 2019. Loss of ent1 increases cell proliferation in the annulus fibrosus of the intervertebral disc. J. Cell. Physiol. 234, 13705–13719. https://doi.org/10.1002/jcp.28051.

Warraich, S., Bone, D.B., Quinonez, D., Ii, H., Choi, D.-S., Holdsworth, D.W., et al., 2013. Loss of equilibrative nucleoside transporter 1 in mice leads to progressive ectopic mineralization of spinal tissues resembling diffuse idiopathic skeletal hyperostosis in humans. J. Bone Miner. Res. 28, 1135–1149. https://doi.org/10.1002/jbmr.1826.

Weijs, W., 1975. Mandibular movements of the albino rat during feeding. J. Morphol. 145, 107–124. https://doi.org/10.1002/jmor.1051450107.

Weinberger, A., 1954. The clinical significance of hypercementosis. Oral Surg. Oral Med. Oral Pathol. 7, 79–87. https://doi.org/10.1016/0030-4220(54)90255-8.

Weinfeld, R.M., Olson, P.N., Maki, D.D., Griffiths, H.J., 1997. The prevalence of diffuse idiopathic skeletal hyperostosis (DISH) in two large American Midwest metropolitan hospital populations. Skelet. Radiol. 26, 222–225. https://doi.org/10.1007/s002560050225.

Westerveld, L.A., van Ufford, H.M.W.Q, Verlaan, J.-J., Oner, F.C., 2008. The prevalence of diffuse idiopathic skeletal hyperostosis in an outpatient population in The Netherlands. J. Rheumatol. 35, 1635–1638.

Wynn, T.A., 2008. Cellular and molecular mechanisms of fibrosis. J. Pathol. 214, 199–210. https://doi.org/10.1002/path.2277.